Journal of Biomedical Optics

BiomedicalOptics.SPIEDigitalLibrary.org

Performance characteristics of an interventional multispectral photoacoustic imaging system for guiding minimally invasive procedures

Wenfeng Xia
Daniil I. Nikitichev
Jean Martial Mari
Simeon J. West
Rosalind Pratt
Anna L. David
Sebastien Ourselin
Paul C. Beard
Adrien E. Desjardins

SPIE.

Journal of Biomedical Optics 20(8), 086005 (August 2015)

Performance characteristics of an interventional multispectral photoacoustic imaging system for guiding minimally invasive procedures

Wenfeng Xia,[a,*,†] Daniil I. Nikitichev,[a,†] Jean Martial Mari,[a] Simeon J. West,[b] Rosalind Pratt,[c] Anna L. David,[c] Sebastien Ourselin,[d] Paul C. Beard,[a] and Adrien E. Desjardins[a]
[a]University College London, Department of Medical Physics and Biomedical Engineering, Gower Street, London WC1E 6BT, United Kingdom
[b]University College Hospital, Department of Anaesthesia, Main Theatres, Maple Bridge Link Corridor, Podium 3, 235 Euston Road, London NW1 2BU, United Kingdom
[c]University College London, Institute for Women's Health, 86-96 Chenies Mews, London WC1E 6HX, United Kingdom
[d]University College London, Center for Medical Imaging Computing, Gower Street, London WC1E 6BT, United Kingdom

Abstract. Precise device guidance is important for interventional procedures in many different clinical fields including fetal medicine, regional anesthesia, interventional pain management, and interventional oncology. While ultrasound is widely used in clinical practice for real-time guidance, the image contrast that it provides can be insufficient for visualizing tissue structures such as blood vessels, nerves, and tumors. This study was centered on the development of a photoacoustic imaging system for interventional procedures that delivered excitation light in the ranges of 750 to 900 nm and 1150 to 1300 nm, with an optical fiber positioned in a needle cannula. Coregistered B-mode ultrasound images were obtained. The system, which was based on a commercial ultrasound imaging scanner, has an axial resolution in the vicinity of 100 μm and a submillimeter, depth-dependent lateral resolution. Using a tissue phantom and 800 nm excitation light, a simulated blood vessel could be visualized at a maximum distance of 15 mm from the needle tip. Spectroscopic contrast for hemoglobin and lipids was observed with *ex vivo* tissue samples, with photoacoustic signal maxima consistent with the respective optical absorption spectra. The potential for further optimization of the system is discussed. [DOI: 10.1117/1.JBO.20.8.086005]

Keywords: photoacoustic imaging; ultrasound imaging; spectroscopy; interventional procedures; image guidance.

Paper 150187R received Mar. 20, 2015; accepted for publication Jul. 15, 2015; published online Aug. 11, 2015.

1 Introduction

Device guidance is of paramount importance for minimally invasive procedures in order to identify procedural targets and to avoid complications. These procedures include nerve blocks, central venous catheterizations, tumor biopsies/ablations, and fetal interventions.[1–4] Ultrasound (US) imaging is widely used for real-time guidance.[5] However, the structural contrast that this modality provides has insufficient sensitivity and specificity to reliably identify tissue targets in many clinical contexts.

Optical reflectance spectroscopy (ORS) probes can provide contrast for absorption and scattering that can be used to differentiate certain soft tissue targets. As such, they have been used for guiding nerve blocks and biopsies in previous studies.[6–9] ORS probes developed to date typically have very limited spatial resolution. For instance, ORS probes that comprise one optical fiber for transmission and a second for reception provide measurements that derive from a single tissue volume, with a sensing depth that is similar to the inter-fiber separation.[10]

Photoacoustic (PA) imaging and conventional US imaging differ in terms of the sources of US waves. In the latter, US waves are transmitted by electrical transducer elements in the imaging probe located at the tissue surface, whereas in the former, US waves are generated inside tissues by light pulses. With PA imaging, the US generation process involves absorption of a light pulse by tissue chromophores, followed by a rapid and localized temperature increase.[11,12] Importantly, the attenuation and spatial distortions of US waves as they propagate through tissue are typically much lower than those of light waves. As PA and US images can be acquired with the same US transducer elements, they can be inherently coregistered. A hybrid US-PA system can, therefore, provide both structural information from US imaging and contrast for tissue chromophores from PA imaging.[13,14]

There is an increasing interest in the use of PA imaging for the guidance of interventional procedures.[15–19] Kim et al.[15] reported a PA imaging system for the guidance of sentinel lymph node biopsies. In their system, which had been modified from a commercial US system, light delivery was provided by a bifurcated optical fiber bundle integrated with the US probe imaging at the tissue surface. One challenge with this light delivery configuration is to achieve sufficient PA signals at depths of several centimeters.[20] To address this challenge, Piras et al.[16] developed a PA imaging system, which they termed "photoacoustic needle," for breast biopsy guidance in which light was delivered inside tissue through an optical fiber embedded in a biopsy needle. However, with the use of a single excitation light wavelength (1064 nm), it is likely to provide limited specificity for tissue targets.

*Address all correspondence to: Wenfeng Xia, E-mail: wenfeng.xia@ucl.ac.uk

†These authors contributed equally to the work.

1083-3668/2015/$25.00 © 2015 SPIE

In this study, we developed an interventional PA imaging system with multiple excitation wavelengths to guide minimally invasive procedures. The light is delivered inside tissue, using a fiber positioned in an injection needle; US detection is provided by a commercial US linear array imaging probe. Performance characteristics of the system, such as resolution and imaging depth are evaluated using tissue-mimicking phantoms. The feasibility of multispectral PA imaging is demonstrated using *ex vivo* tissue samples, including human blood cells, porcine fat, and a human placenta.

2 Materials and Methods

2.1 *Instrumentation*

2.1.1 *Light source and light delivery*

An optical parametric oscillator (OPO) system (VersaScan L-532, VersaScan L-532, GWU-Lasertechnik, Erftstadt, Germany) pumped by an Nd:YAG laser (repetition rate: 10 Hz; Quanta-Ray, INDI-40-10, Spectra-Physics, Santa Clara, California) was used as the PA excitation light source (Fig. 1). The OPO has two outputs: the signal (700 to 900 nm) and the idler (1100 to 2200 nm). Wavelength tuning was performed with a motorized crystal controlled by a custom Labview program (National Instruments, Berkshire, United Kingdom). The OPO outputs were focused onto separate silica–silica optical fibers with 910 μm cores (Thorlabs, Newton, New Jersey) with achromatic doublet lenses (focal length: 50 mm; AC254-050-B, and AC254-050-C, Thorlabs). One of these two optical fibers directed light at an optical fiber of the same type, with its distal section positioned in the cannula of a 14 gauge needle (Fig. 1). Within tissue phantoms and *ex vivo* tissue, the fiber tip was positioned 2 mm out of the needle tip to mitigate imaging artifacts from the metal needle, including PA signal generation from the needle and US reverberations within the needle cannula.

A small fraction of the OPO outputs was deflected to photodetectors to measure pulse-to-pulse energy fluctuations and to provide optical triggering. This deflection was performed by glass windows that were positioned proximal to the focusing lenses. The outputs of the photodetectors were digitized by an oscilloscope (DPO3000, Tektronix, Oregon) at 2.5 GS/s; this oscilloscope also detected the rising edge of each laser pulse and converted it to a trigger signal. The output pulse energies at the distal end of the fiber were measured separately (H410/AC2501, Scientech, Tukwila, Washington); they varied from 4 to 6 mJ over the wavelength ranges used in all experiments.

2.1.2 *Ultrasound detection*

Ultrasound detection [Fig. 1(a)] was performed with a commercial US imaging system (SonixMDP, Analogic Ultrasound, Richmond, British Columbia, Canada) that was operated in its research mode. The system used a linear array imaging probe (L14-5/38, 128-element, 300 μm pitch, Analogic

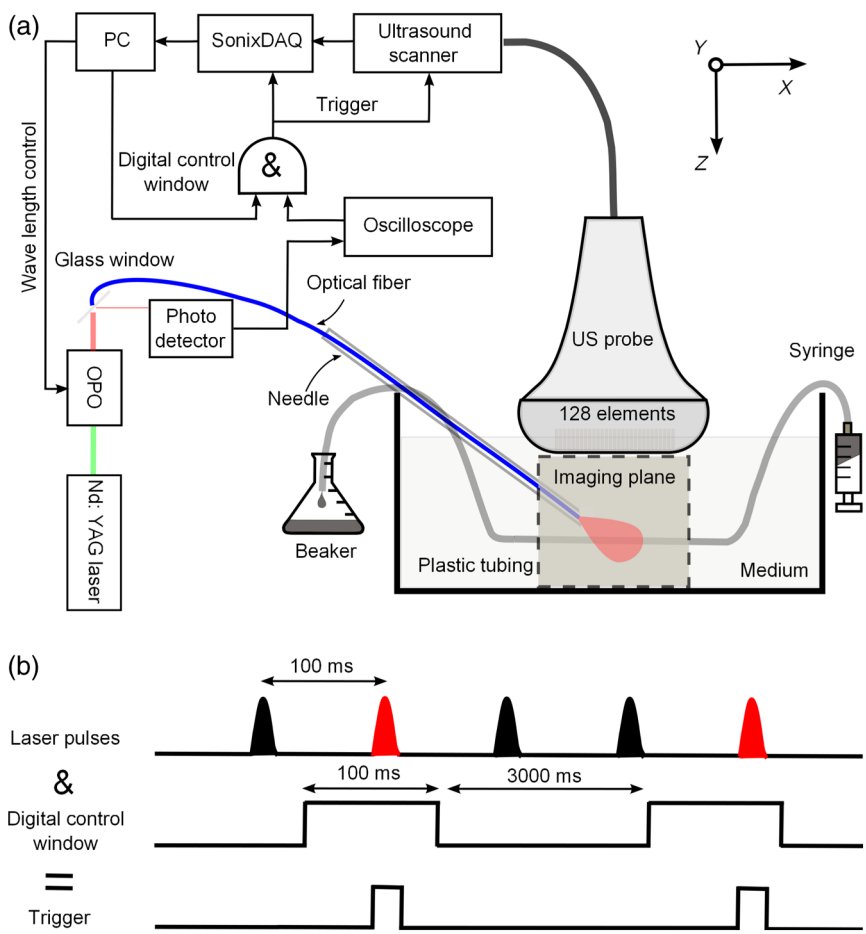

Fig. 1 (a) Schematic of the interventional multispectral photoacoustic imaging system and (b) a temporal sequence showing how triggering and pulse gating were performed using a digital control window.

Ultrasound). Pre-beamformed channel data from the transducer element were sampled at 40 MHz with a 12-bit analog-to-digital converter by a 128-channel data acquisition system (SonixDAQ, Analogic Ultrasound)[21] and were sent to a personal computer for postprocessing. Two amplification stages were performed with built-in amplifiers. A first amplification stage boosted the incoming signals from each channel using a set of low noise amplifiers (LNA). The amplification at the first stage could be set using parameter values of 0, 1, and 2, which corresponded to amplifications of 16, 18, and 21 dB, respectively. Amplification at the second stage was performed using voltage-controlled amplifiers (VGA); parameter values 0, 1, 2, and 3 corresponded to amplification levels of 21, 24, 27, and 30 dB, respectively. The signal-to-noise ratios (SNR) for a representative transducer element channel of the DAQ system for different gain settings were measured using a single piezoelectric transducer element (PA080, Precision Acoustics, Dorset, United Kingdom) as a 10 MHz US source. The highest SNR was achieved when both LNA and VGA values were set to 2 (Fig. 2); these settings were applied for all experiments.

2.1.3 *System synchronization*

The acquisitions of the US and PA images were triggered by light pulses. With the OPO operating continuously at 10 Hz, acquisitions were controlled by the Labview program via a digital I/O card (NI-USB-6501, National Instruments). As illustrated in Fig. 1(b), this scheme was realized using a logic AND gate (CD74HCT08E, Texas Instruments, Dallas, Texas) with two input signals: the optical trigger and the digital control window signal. The optical trigger was derived from an oscilloscope (DPO3000, Tektronix, Oregon) with a photodiode signal as its input. The control window signal was 100 ms in duration; the oscilloscope trigger hold-off ensured that only one pulse occurred within the window. When the SonixDAQ was triggered, 128 channels of radio frequency (RF) data from the transducer elements of the US imaging probe were acquired. After completion of PA image acquisition, the US machine performed individual line scans for standard B-mode US imaging. In this manner, a pair of PA and US images was acquired in an interleaved manner for each trigger event. A custom program, developed with the cross-platform application framework Qt,[22] controlled the acquisition parameters, such as the gain settings, the acquisition delay, and the acquisition depth for both PA and US imaging. For each wavelength, 15 PA and US images were acquired with a speed of 15 frames per minute.

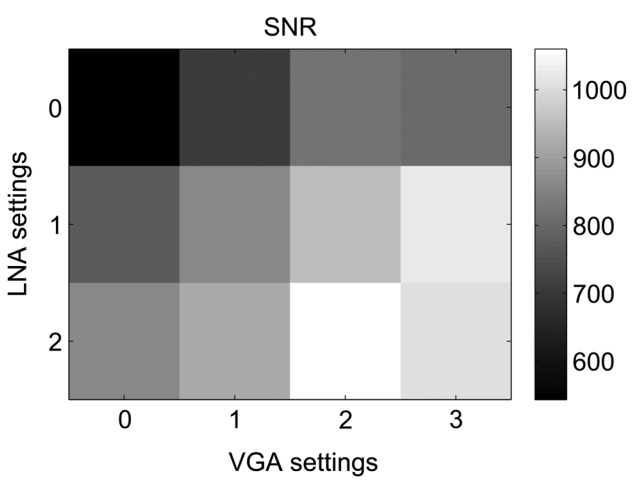

Fig. 2 The effect of different gain settings on the photoacoustic signal-to-noise ratio (SNR). LNA, low noise amplifier; VGA, voltage controlled amplifier. LNA parameter values 0, 1, and 2 correspond to amplifications of 16, 18, and 21 dB; VGA parameter values 0, 1, 2, and 3 correspond to amplifications of 21, 24, 27, and 30 dB, respectively.

2.1.4 *Image reconstruction*

Immediately after an acquisition of RF data for PA imaging, image reconstruction was performed using a custom delay-and-sum beam-forming algorithm. The B-mode US images were reconstructed using electronic beamforming, and the post-beamformed data were displayed alongside the PA images. As such, reconstructed PA and US images were displayed in real time. Offline image reconstruction of PA images was performed using a Fourier-domain reconstruction algorithm,[23] which was implemented with the k-Wave MATLAB® toolbox.[24]

2.2 *Resolution*

A 7-μm carbon fiber (Quorum Technologies Ltd., East Sussex, United Kingdom) was used as a point target for spatial resolution measurements [Fig. 3(a)]. The carbon fiber was perpendicular to the imaging plane in a water tank illuminated by an Nd:YAG laser (wavelength 1064 nm; pulse width 2 ns; pulse energy 30 μJ, SPOT-10-500-1064, Elforlight, United Kingdom) that was coupled into a 600 μm optical fiber (Thorlabs). To measure the spatial resolution at different locations relative to the US probe, the US probe was translated relative to the target, with the optical fiber fixed in position [Fig. 3(a)]. Resolution measurements were obtained at eight depths for two lateral positions. The full width at half maximum values of the axial and lateral profiles across the center of the reconstructed objects were used as measures of the spatial resolution.

2.3 *Imaging Depth*

The relationship between the PA signal amplitude and the distance between the excitation light source and the imaging target (referred to in this study as the imaging depth) was evaluated with a tissue-mimicking phantom. A soft polymer tube (inner diameter: 2 mm) filled with India ink (Higgins, Essex, United Kingdom) that was diluted to 0.5% was placed horizontally in the imaging plane to mimic a blood vessel. The absorption spectrum of the ink dilution was measured using a custom transmission spectrophotometer based on a visible near-infrared (NIR) spectrometer (Maya Pro, Ocean Optics, Milan, Italy). The measured absorption coefficient (μ_a) was 0.45 mm^{-1} at 800 nm, which is consistent with measurements of human blood.[25] As shown in Fig. 1(a), the US transducer and the ink tube were surrounded with 1% Intralipid dilution to simulate the optical scattering of biological tissues.[26,27] To avoid the confounding effects of PA excitation by the metal needle, a bare optical fiber was used to deliver excitation light. To estimate the imaging depth, the fiber was withdrawn along the fiber axis from a fiber-target distance of 1 to 10 mm in steps of 1 mm. PA images at three wavelengths (750, 800, and 850 nm) were acquired for each distance. Since the relative position of the object and the US probe remained the same, the amplitude of the reconstructed

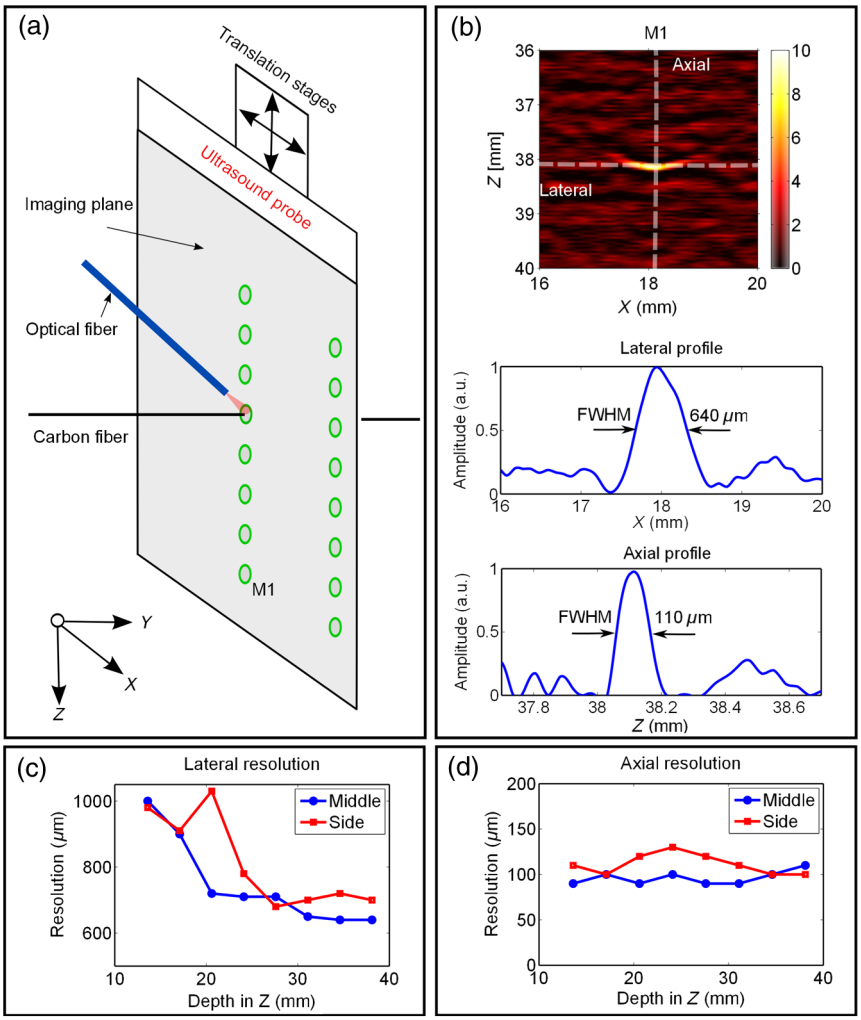

Fig. 3 Spatial resolution of the photoacoustic images. (a) Schematic illustration of the measurement geometry. (b) Upper: reconstructed photoacoustic image of the carbon fiber located 38 mm (M1) from the ultrasound probe. Lower: lateral and axial profiles through the center of the reconstructed target, and the corresponding full width at half maximum values as measured of the lateral and axial resolution. The lateral and axial resolution values at different depths for target positions at the center and the edge of the image plane are provided in (c) and (d).

PA image (in linear units) at the target, S_{ROI}, was assumed to be proportional to the generated pressure $P(\lambda)$.

$$S_{\mathrm{ROI}}(\lambda) = \alpha P(\lambda), \tag{1}$$

where α is a constant scaling factor and λ is the PA excitation wavelength. $P(\lambda)$ can be expressed as[28]

$$P(\lambda) = \Gamma \mu_{\mathrm{a,ROI}}(\lambda)\Phi(\lambda), \tag{2}$$

where $\Phi(\lambda)$ is the local fluence at the target, which was modeled as[28–30]

$$\Phi(\lambda) = Q(\lambda)\frac{\exp[-\mu_{\mathrm{eff}}(\lambda)d]}{4\pi D(\lambda)d}, \tag{3}$$

where Q is the energy of a light pulse delivered to tissue at the fiber tip, d is the fiber-target distance, and λ is the optical wavelength. The optical properties are denoted as follows: μ_{eff} and D are the effective attenuation coefficient and the diffusion length of the medium, respectively; $\mu_{\mathrm{a,ROI}}$ and Γ are the absorption coefficient and the Grüneisen coefficient of the target. Equations (1) to (3) can be written as

$$S_{\mathrm{ROI}}(\lambda) = \beta(\lambda)\mu_{\mathrm{a,ROI}}\frac{\exp[-\mu_{\mathrm{eff}}(\lambda)d]}{d}, \tag{4}$$

where β is constant with respect to the distance and does not depend explicitly on μ_{eff}. To estimate μ_{eff}, Eq. (4) was fit to the experimental data using a nonlinear least squares algorithm with β, d, and μ_{eff} as free parameters. The maximum achievable distance at which a blood vessel of a given size could be detected with a particular excitation wavelength was obtained by extrapolating measured average PA signals toward the noise floor, using Eq. (4).

2.4 *Ex Vivo Measurements*

2.4.1 *Human blood cells and porcine fat*

To obtain a preliminary indication of the potential of the system for guiding nerve blocks for which fat-rich nerves and

hemoglobin-rich blood vessels are tissue structures of interest, multispectral PA imaging was performed on fat and expired human blood cells (University College London Hospital Blood Transfusion Laboratory). Porcine fat was melted to temperatures in the range of 60 to 70°C and injected into a polymer tubing (inner diameter: 2.80 mm, outer diameter: 3.15 mm, Morcap56, Paradigm Optics, Vancouver) with a syringe [Fig. 1(a)]. Red blood cells were injected into a second polymer tube. Prior to experiments, the RBCs were exposed to air. The oxygen saturation of these RBCs was estimated to be >90%.[31] The two polymer tubes were placed in parallel between two layers of chicken breast tissue. A 24 gauge needle was inserted through the chicken layers to mechanically stabilize them and to prevent water from surrounding the tubes. PA imaging was performed at two wavelength ranges: 750 to 900 nm (OPO signal) and 1150 to 1300 nm (OPO idler).

Image processing of multispectral images was performed by averaging over regions of interest (ROIs). A 4 mm × 4 mm ROI that encompassed the fat-filled tube (ROI_f) and a second that encompassed the RBC-filled tube (ROI_b) were defined, and the average PA image amplitude values S_{ROI} were calculated from these ROIs for each wavelength. A relative absorption spectrum of the target was estimated by a simple optical inversion derived from Eq. (1).

$$\mu_{\mathrm{a,ROI}}(\lambda) = \frac{d}{\beta(\lambda)\exp[-\mu_{\mathrm{eff}}(\lambda)d]} S_{\mathrm{ROI}}(\lambda), \tag{5}$$

with β estimated from Eq. (4) and $\exp[-\mu_{\mathrm{eff}}(\lambda)d]/d$ is a normalizing term to compensate the fluence variations as a function of d.

2.4.2 *Human placenta*

In addition to guiding nerve blocks, the system developed in this study could be used to guide treatments of twin-to-twin transfusion syndrome, where identification of blood vessels in the placenta is of critical importance.[32] To obtain a preliminary indication of the system's potential for this application, multispectral PA imaging across an excitation wavelength range of 750 to 900 nm was performed on a term human twin placenta [Fig. 4(a)]. This placenta was collected after a Caesarean section delivery at University College London Hospital with written informed consent from the mother, as approved by the Joint Committees on the Ethics of Human Research (08/H0817/07 amniotic fluid and placental stem cells). After delivery, the umbilical cords were immediately clamped to preserve the maximum amount of blood inside the placental fetal vasculature. A block of transparent agar gel (3 w/w% in water; thickness: 2.5 cm) was sandwiched between the US probe and the placenta as a US coupling medium. The gel was used to simulate the amniotic fluid within the gestation sac and to prevent the diffusion of blood out of the placenta. The needle was inserted at an angle of ~45 deg to the fetal surface of the placenta. The distance between the needle tip and the placenta surface was 5 mm. Absorption spectra of surface placental vessels were obtained using the approximation $\mu_{\mathrm{eff}} = 0$ since the attenuation of the

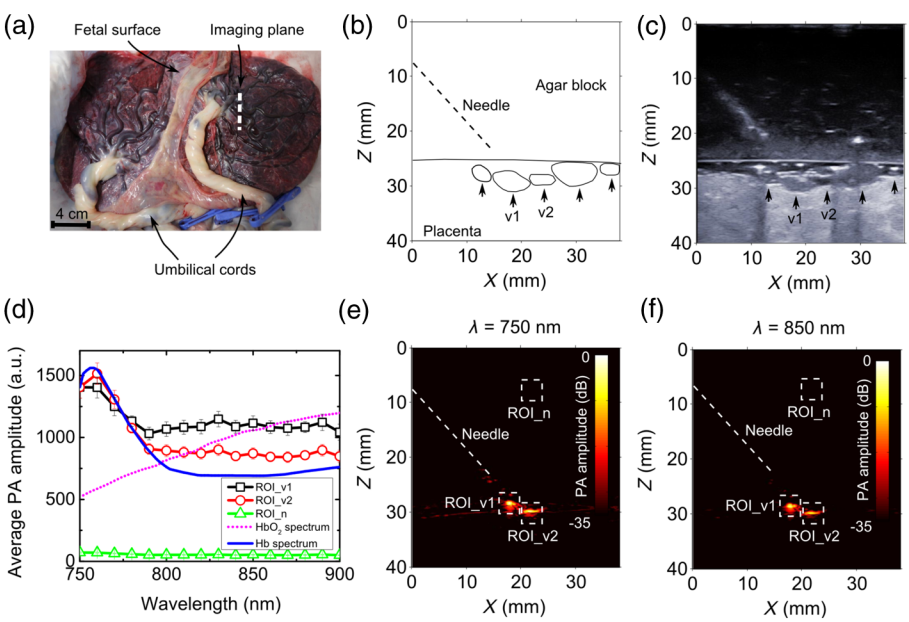

Fig. 4 Multispectral photoacoustic images of the human placenta. (a) Photograph of the human twin placenta, with the location from which ultrasound and photoacoustic images were acquired, indicated with a white dashed line. An ultrasound image of the placenta together with the structure outlines are shown in (b) and (c). Coregistered photoacoustic images at wavelengths of 750 and 850 nm are shown in (e) and (f). Two veins [v1 and v2 in (b) and (c)] are clearly visible in the photoacoustic images. Average photoacoustic amplitudes for regions of interest (v1: ROI_v1; v2: ROI_v2; background noise: ROI_n) indicated in (e) and (f) are compared with the absorption spectra of oxygenated and deoxygenated blood in (d) for wavelengths from 750 to 900 nm. The oxygenated and deoxygenated blood spectra are normalized to the measured average photoacoustic amplitudes at 750 nm. The photoacoustic signal amplitudes in (d) are presented as averages over 15 image frames, with error bars representing standard deviations.

agar gel in the wavelength range of 750 to 900 nm was assumed to be negligible.

3 Results

The carbon fiber target used for spatial resolution measurements was clearly visible on reconstructed PA images at depths of up to 38 mm. The point spread function was approximately ellipsoidal, with the shorter axis in the axial dimension [Fig. 3(b)]. The lateral resolution improved with depth, with values ranging from 1000 μm at a depth of 12 mm to 600 to 700 μm at a depth of 38 mm. It was also larger at the side of the image [Fig. 3(c)] in the range of 900 to 1000 μm at the edges. The axial resolution was nearly constant at depths of up to 38 mm and across lateral positions, with values in the vicinity of 100 μm [Fig. 3(d)].

With the phantom used to characterize the dependency of PA signal on the needle-target distance, prominent PA signals were observed from both sides of the India ink filled tube target, in a region illuminated by the fiber [Fig. 5(a)]. The PA signal from the fiber itself was also apparent. Good spatial correspondence between the structures on the PA and US images was observed [Figs. 5(a)–5(d)]. On US imaging, the fiber tip and its distance to the tube could be clearly visualized. As the distance between the illumination fiber and the tube decreased from 5 to 1 mm, the spatial region from which a prominent PA signal was obtained decreased in lateral size from ~2 to 0.5 cm [Figs. 5(a) and 5(c)]. PA signal amplitudes averaged from a 4 mm × 4 mm ROI that encompassed the tube, S_{ROI}, and decreased as the distance between the illumination fiber and the tube, d, increased [Fig. 5(e)]. The relationship between S_{ROI} and d was very similar for the three excitation wavelengths: 750, 800, and 850 nm. For each wavelength, this relationship was in excellent agreement with that predicted by Eq. (4), with the parameter μ_{eff} as a free variable. The fitted values of μ_{eff}, which were in the range of 0.08 to 0.11 mm^{-1} for the three excitation wavelengths, were within 30% of values obtained from a previous study[26,33] (Table 1).

With the *ex vivo* tissue phantom comprising two layers of chicken breast, the tubes with oxygenated blood and with fat were visible with PA imaging [Figs. 6(a) and 6(b)]. At a wavelength of 800 nm, only the tube with oxygenated blood was visible. At 1210 nm, both the tubes with oxygenated blood and with fat were visible. At both wavelengths, PA signal was also observed at the fiber tip. This signal was higher at 1210 nm than at 800 nm; at the former wavelength, water absorption is more prominent.[33] The structural information provided by the US image facilitated interpretation of the PA images [Fig. 6(c)]; however, the tubes were not clearly visible in the US images due to the presence of chicken breast layers. As the wavelength increased from 750 to 900 nm, the PA signal from the blood-filled tube increased by 120% [Fig. 6(d)]. The wavelength dependence of this PA signal corresponded well to the optical absorption spectrum of oxygenated blood. Over this wavelength range, the PA signal from the lipid-filled tube was approximately constant and close to the PA image noise level, which is consistent with low optical absorption by lipid.[14,35] For wavelengths in the range of 1150 to 1300 nm, PA signal amplitudes above the noise floor corresponded well to the optical absorption spectrum of lipid measured in a previous study.[36] In particular, the peak PA signal amplitude occurred at 1210 nm [Fig. 6(e)], which coincides with an optical absorption peak of lipid.[36] Over this wavelength range, the PA signal amplitude from the blood-filled tube had a smaller peak at 1210 nm.

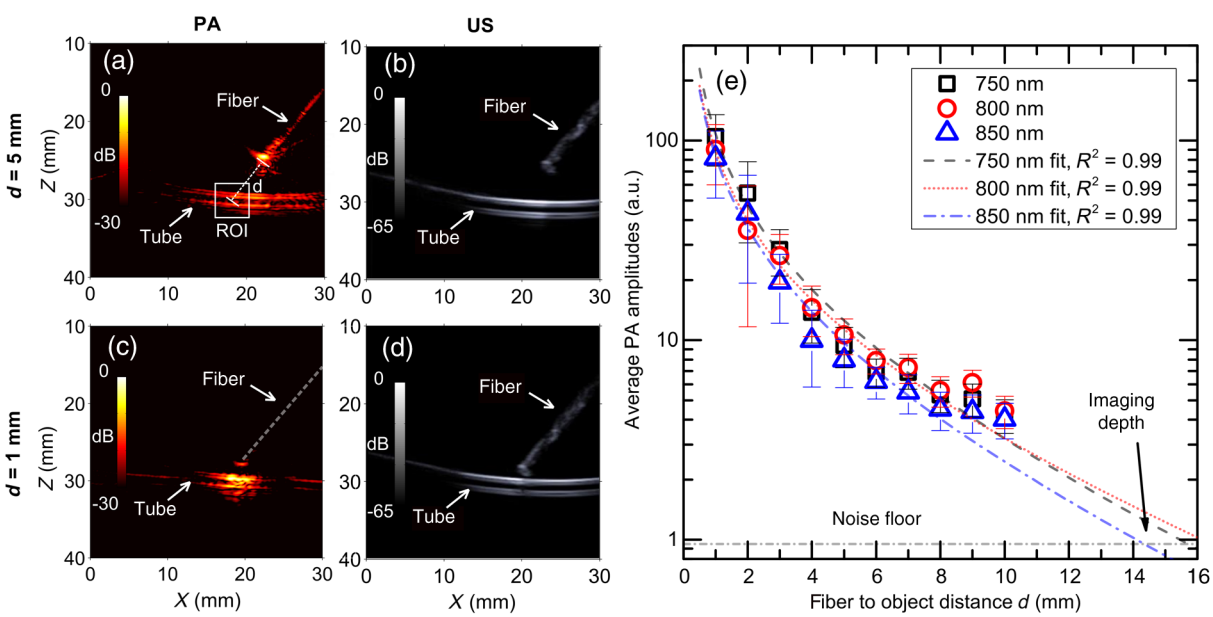

Fig. 5 Coregistered photoacoustic and ultrasound images were acquired, with the distance between the distal end of the fiber optic and the polymer tube filled with India ink, d, varied from 1 to 10 mm. Examples are shown for $d = 5$ mm [(a) and (b)] and for 1 mm [(c) and (d)]. The colorbars in (a) and (c), and (b) and (d) correspond to photoacoustic and ultrasound image amplitudes, respectively. Average photoacoustic amplitudes (S_{ROI}) in a 4 mm × 4 mm region of interest indicated in (a) for wavelengths 750, 800, and 850 nm are plotted for d from 1 to 10 mm in (e). The data in (e) represent the average values from 15 image frames; the error bars represent the standard deviations. Equation (4) is used to fit the measured S_{ROI} values for each wavelength and compare with the measured data. The intersections of the fitted curves and the noise floor indicate a maximum imaging depth of ~15 mm for the detection of blood vessels. The estimated μ_{eff} values from curve fitting are compared with literature values in Table 1.

Table 1 Effective attenuation coefficient μ_{eff} of the Intralipid 1% solution used in the tissue phantom. Values of μ_{eff} (values ±95% confidence level bounds) estimated from Eq. (4) are compared with previous studies, with the reduced scattering coefficient $\mu'_{s,m}$ taken from Ref. 26 and the absorption coefficient $\mu_{a,m}$ approximated by that of water obtained from Ref. 33. All values are in mm^{-1}.

	Estimated			Literature[26,33]		
Wavelength	750 nm	800 nm	850 nm	750 nm	800 nm	850 nm
μ_{eff}	0.13 ± 0.067	0.11 ± 0.068	0.13 ± 0.061	0.095	0.080	0.11

At wavelengths >1250 nm, where water absorption is prominent, the PA signal from the lipid-filled tube approached the noise floor, and that from the blood-filled tube remained significantly higher than the noise floor. Variations in the PA images as the wavelength was increased were visually apparent. With excitation wavelengths in the range of 750 to 900 nm, a signal from the blood-filled tube was permanently visible, while the signal from the lipid-filled tube was invisible (Video 1). With excitation wavelengths in the range of 1150 to 1300 nm, the visibility of the lipid-filled tube was particularly high at wavelengths in the vicinity of 1210 nm, while the visibility of the blood-filled tube remained approximately constant (Video 2).

With the human placenta, two major surface veins that were visually identified [Fig. 4(a)] were clearly apparent with both PA [Figs. 4(e) and 4(f)] and US imaging [V1, V2 in Figs. 4(b) and 4(c)]. Both PA and US images had good spatial correspondence. With excitation wavelengths in the range of 750 to 900 nm, the PA signal amplitudes from the blood vessels decreased with wavelength [Fig. 4(d)], with a peak signal amplitude at ~760 nm. This wavelength dependency was similar to the

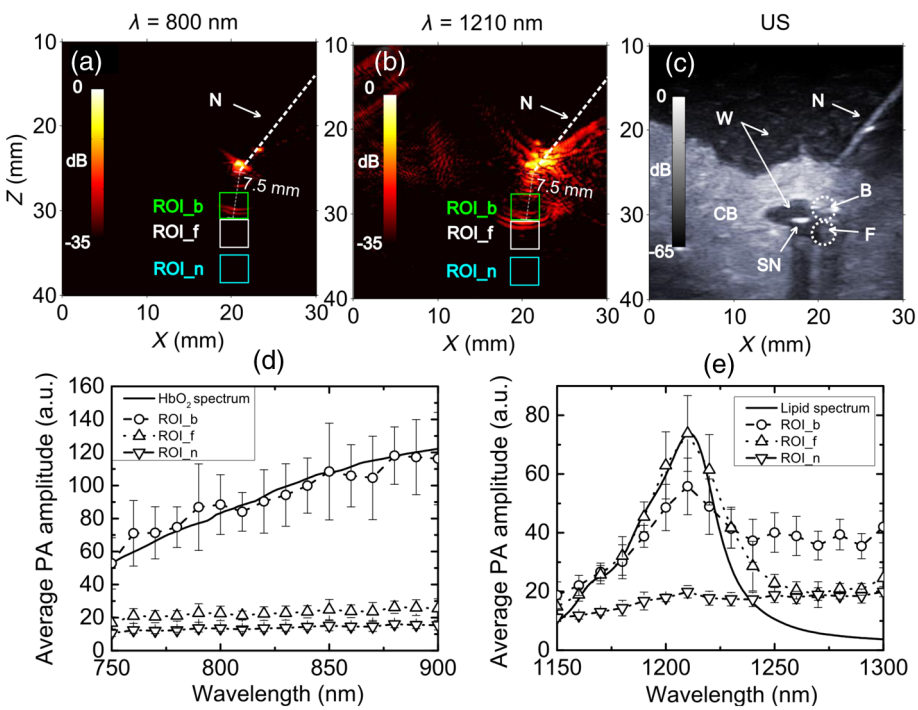

Fig. 6 Multispectral photoacoustic images of the blood and fat samples. Photoacoustic images of the two tubes filled with oxygenated blood and fat at wavelengths of 800 and 1210 nm are shown in (a) and (b). Coregistered ultrasound image of the tubes are shown in (c). The colorbars in (a) and (b), and (c) correspond to photoacoustic and ultrasound image amplitudes, respectively. Photoacoustic images corresponded well to the ultrasound images. Photoacoustic images generated with excitation wavelengths ranging from 750 to 900 nm are shown in Video 1, and from 1150 to 1300 nm are shown in Video 2. Fluence-compensated average photoacoustic amplitudes for regions of interest (blood: ROI_b; fat: ROI_f; background noise: ROI_n) indicated in (a) to (c) are compared with the absorption spectra of oxygenated blood and fat in (d) and (e) for excitation light wavelengths from 750 to 900 nm and from 1150 to 1300 nm, respectively. The oxygenated blood and fat spectra are normalized to the measured average photoacoustic amplitudes at 750 and 1210 nm, respectively, for comparison. The photoacoustic signal amplitudes are averaged over 15 image frames; the error bars represent standard deviations. Good agreement between the measured spectra of oxygenated blood and fat and previous estimates were observed.[34] N, needle; W, water; CB, chicken breast; SN, second needle; B, blood; F, fat. (Video 1, mov, 374 KB [URL: http://dx.doi.org/10.1117/1.JBO.XX.XX.XXXXXX.1] and Video 2, mov, 471 KB) [URL: http://dx.doi.org/10.1117/1.JBO.XX.XX.XXXXXX.2].

optical absorption spectrum of deoxygenated blood [Fig. 4(c)].[25] Over this wavelength range, PA signal amplitudes from both vessels were much higher than the background noise floor [Fig. 4(d)].

4 Discussion

This study was centered on the development and characterization of a system for performing multispectral PA imaging in which excitation light was delivered through the cannula of an injection needle. The system has a strong potential to provide contrast for vasculature and nerves during minimally invasive procedures, using two NIR wavelength ranges for excitation light in which hemoglobin and lipids have prominent optical absorption. The coregistered B-mode US images provided structural information that facilitated interpretation of the PA images.

Excitation light delivery with optical fibers positioned within an interventional device could be used to optimize PA signal generation from tissue structures of interest. Indeed, as the attenuation of US is significantly lower than that of light in the NIR, this light-delivery scheme could allow multispectral PA images to be obtained at depths that are unattainable with light delivery at the tissue surface. One limitation of delivering light through a needle cannula is that the needle itself can be a source of PA signal. As noted in a previous study,[34] this source of US can take place when the excitation light is incident on the needle, either directly or after scattering in tissue, and additional artifacts can result from US reverberations within the needle cannula. In this study, these effects were found to be mitigated when the optical fiber that delivered excitation light was pushed around 2 mm beyond the distal tip of the needle. In clinical practice, the optical fiber would most likely need to be retracted to within the lumen of the needle to avoid the friction between it and the tissue during insertions. Out-of-plane insertions, in which the needle is inserted toward the imaging plane rather than within it, may be preferential from the standpoint of minimizing signal contributions from the needle. Clutter reduction algorithms could be applied to mitigate the image artifacts associated with the needle tip.[37,38]

From a clinical translation standpoint, the large excitation light fluences at the needle tip in this study are a concern. With a maximum pulse energy of 6 mJ, the fluence at the fiber tip was 923 mJ/cm^2. This fluence is much larger than the maximum permissible exposure (MPE) of 20 mJ/cm^2 for NIR light at the skin surface.[39] This concern can be addressed in two ways. First, light could be delivered into tissue so that the fluence is within the MPE at all locations. For example, cylindrical fiber diffusers developed for photodynamic therapy[40] could be used. Alternatively, US imaging probes could be developed by including additional US detectors with dimensions optimized for high sensitivity in reception mode,[20] so that smaller pulse energies are required to achieve detectable PA signals. Ultimately, the current MPE values may be found to be overly conservative when applied to weakly-absorbing tissues within the body.[41]

The spatial resolution of the PA images is likely to be sufficient for many minimally invasive procedures, given that the lateral and axial widths of the measured point spread functions were smaller than the outer diameters of the injection needles. As with B-mode US images, the limited bandwidth of the piezoelectric elements resulted in band-pass filtering of the RF data, so that PA imaging signals derived primarily from spatial changes in optical absorption. This filtering effect was apparent in the images of the blood- and lipid-filled tubes (Fig. 6). Deconvolution algorithms could be useful to partially compensate for frequency-filtering effects.[42,43]

With one PA image acquired for each excitation light pulse, the PA imaging frame rate was intrinsically limited by the OPO repetition rate. At a particular excitation wavelength, the rate at which PA images were displayed was a factor of 40 beneath this limit. Two factors that limited the image display rate were the transfer of raw RF data to memory and to disk and the reconstruction of images. The latter factor could be addressed with the use of graphics processing units.[24] With multispectral imaging, the rate at which PA image frames with different wavelengths could be acquired was intrinsically limited by the wavelength-tuning speed of the OPO. In this study, there were additional time delays associated with synchronizing PA image acquisition with the wavelength-tuning motor, which could be partially alleviated by the use of an externally triggered laser.

The PA imaging depth of the system depended on several factors, including the wavelength of the excitation light and the concentrations of the tissue chromophores. Using known wavelength-dependencies of the optical properties of tissues and the optical absorption spectra of particular chromophores, the results of this study can be extrapolated to predict the imaging depth that could be attained in other contexts, for instance, by using the optical properties of a 1% Intralipid dilution.[26,36,44]

With the *ex vivo* tissue phantom, both water and lipid absorption contributed to PA spectra in the wavelength range from 1150 to 1300 nm. The shape of the PA spectrum from the lipid-filled tube was very similar to that of the optical absorption spectrum of lipid. Given that PA signals derive from spatial differences in chromophore concentrations, it can be surmised that the PA spectrum originated primarily from the boundary between the tube wall (which is assumed to have negligible absorption) and the lipid interior, and that contributions from the tube wall and water surrounding the tube were small. In the PA spectrum from the blood-filled tube, spectroscopic features from both water and lipid were apparent, with the former manifesting as a detectable signal beyond 1250 nm, and the latter as a small absorption peak at 1210 nm. Contributions from water to the PA spectrum may have originated from the boundary between the tube wall and the water within blood. The lipid absorption peak is likely an artifact that arose from the small separation between the blood- and lipid-filled tubes. The background PA signal, which originated from a chicken breast tissue region, did not have spectroscopic features of hemoglobin, water, or lipid.

Two conclusions can be drawn from the PA and US images of the human placenta. First, the similarity between the PA spectra measured from the two veins and the optical absorption spectrum of the deoxygenated blood provides confidence that contrast for oxygen saturation can be obtained. In future studies, iterative, model-based inversion algorithms, such as those discussed in Refs 13, 45, and 46, could be used for quantification. Second, the field of view from which PA contrast can be obtained depends strongly on the illumination conditions. In this study, the limited NA of the fiber and the clarity of the agar gel resulted in substantial illumination of only two of the five surface vessels that were visualized with US in the imaging plane. In an *in vivo* context, the illumination of the placental surface will depend, in part, on the fiber-object distance and the turbidity of the amniotic fluid.[47] For particular ranges of

fiber-object distances, the field of view could be optimized using fiber bundles or lenses.

PA multispectral imaging could play an important role with real-time guidance of minimally invasive procedures, as it can provide molecular information that is complementary to conventional B-mode US images in real time. As many procedural targets are several centimeters beneath the tissue surface, obtaining strong PA signals with light delivery provided at the tissue surface may be very challenging. This study provided indications that excitation light delivery through a needle cannula could be a viable alternative. Reduction of the excitation light fluence at the needle tip and reduction of the contributions of PA signals from the needle must be addressed before studies are performed on human patients. Follow-on *in vivo* imaging studies will be crucial to determine the PA appearances of targets that have hitherto remained beyond the imaging depth of PA imaging systems with surface-based illumination.

Acknowledgments

This work was supported by an Innovative Engineering for Health award by the Wellcome Trust (WT101957) and the Engineering and Physical Sciences Research Council (EPSRC) (NS/A000027/1), by a Starting Grant from the European Research Council (ERC-2012-StG, Proposal 310970 MOPHIM), and by an EPSRC First Grant (EP/J010952/1). ALD is supported by the UCL/UCLH NIHR Comprehensive Biomedical Research Centre. The authors are grateful for the support for obtaining the human placenta provided by Efthymios Maneas of the University College London.

References

1. M. Bluvol et al., "A needle guidance system for biopsy and therapy using two-dimensional ultrasound," *Med. Phys.* **35**, 617–628 (2008).
2. A. G. Randolph et al., "Ultrasound guidance for placement of central venous catheters: a meta-analysis of the literature," *Crit. Care Med.* **24**(12), 2053–2058 (1996).
3. M. Ahmed et al., "Image-guided tumor ablation: standardization of terminology and reporting criteria—10-year update," *Radiology* **273**(1), 241–260 (2014).
4. P. E. Bigeleisen, N. Moayeri, and G. J. Groen, "Extraneural versus intraneural stimulation thresholds during ultrasound-guided supraclavicular block," *Anesthesiology* **110**, 1235 (2009).
5. S. N. Narouze, Ed., "*Atlas of Ultrasound-Guided Procedures in Interventional Pain Management*," Springer, New York (2010).
6. M. Brynolf et al., "Optical detection of the brachial plexus for peripheral nerve blocks: an in vivo swine study," *Reg. Anesth. Pain Med.* **36**, 350–357 (2011).
7. A. E. Desjardins et al., "Epidural needle with embedded optical fibers for spectroscopic differentiation of tissue: ex vivo feasibility study," *Biomed. Opt. Express* **2**(6), 1452–1467 (2011).
8. A. E. Desjardins et al., "Needle stylet with integrated optical fibers for spectroscopic contrast during peripheral nerve blocks," *J. Biomed. Opt.* **16**(7), 077004 (2011).
9. S. H. Tabrizi et al., "Single fiber reflectance spectroscopy on cervical premalignancies: the potential for reduction of the number of unnecessary biopsies," *J. Biomed. Opt.* **18**(1), 017002 (2013).
10. D. Arifler et al., "Spatially resolved reflectance spectroscopy for diagnosis of cervical precancer: Monte Carlo modeling and comparison to clinical measurements," *J. Biomed. Opt.* **11**(6), 064027 (2006).
11. P. C. Beard, "Biomedical photocoustic imaging," *Interface Focus* **1**(4), 602–631 (2011).
12. J. Xia, J. Yao, and L. V. Wang, "Photoacoustic tomography: principles and advances," *PIER* **147**, 1–22 (2014).
13. J. G. Laufer et al., "Quantitative spatially resolved measurement of tissue chromophore concentrations using photoacoustic spectroscopy: application to the measurement of blood oxygenation and haemoglobin concentration," *Phys. Med. Biol.* **52**, 141 (2007).
14. T. J. Allen et al., "Spectroscopic photoacoustic imaging of lipid-rich plaques in the human aorta in the 740 to 1400 nm wavelength range," *J. Biomed. Opt.* **17**(6), 061209 (2012).
15. C. Kim et al., "Handheld array-based photoacoustic probe for guiding needle biopsy of sentinel lymph nodes," *J. Biomed. Opt.* **15**(4), 046010 (2010).
16. D. Piras et al., "Photoacoustic needle: minimally invasive guidance to biopsy," *J. Biomed. Opt.* **18**(7), 070502 (2013).
17. M. A. Lediju Bell et al., "In vivo visualization of prostate brachytherapy seeds with photoacoustic imaging," *J. Biomed. Opt.* **19**(12), 126011 (2014).
18. M. A. Lediju Bell et al., "Transurethral light delivery for prostate photoacoustic imaging," *J. Biomed. Opt.* **20**(3), 036002 (2015).
19. L. Lin et al., "In vivo deep brain imaging of rats using oral-cavity illuminated photoacoustic computed tomography," *J. Biomed. Opt.* **20**(1), 016019 (2015).
20. W. Xia et al., "An optimized ultrasound detector for photoacoustic breast tomography," *Med. Phys.* **40**(3), 032901 (2013).
21. C. C. P. Cheung et al., "Multi-channel pre-beamformed data acquisition system for research on advanced ultrasound imaging methods," *IEEE Trans. Ultrason. Ferroelectr. Freq. Control* **59**(2), 243–253 (2012).
22. http://qt-project.org/ (3 August 2015).
23. K. P. Köstli and P. C. Beard, "Two-dimensional photoacoustic imaging by use of Fourier-transform image reconstruction and a detector with an anisotropic response," *Appl. Opt.* **42**(10), 1899–1908 (2003).
24. B. E. Treeby and B. T. Cox "k-Wave: MATLAB toolbox for the simulation and reconstruction of photoacoustic wave fields," *J. Biomed. Opt.* **15**(2), 021314 (2010).
25. A. Roggan et al., "Optical properties of circulating human blood in the wavelength range 400–2500 nm," *J. Biomed. Opt.* **4**(1), 36–46 (1999).
26. H. J. Van Staveren et al., "Light scattering in Intralipid-10% in the wavelength range of 400–1100 nm," *Appl. Opt.* **30**, 4507–4514 (1991).
27. W. Xia et al., "Poly(vinyl alcohol) gels as photoacoustic breast phantoms revisited," *J. Biomed. Opt.* **16**(7), 075002 (2011).
28. R. O. Esenaliev, A. A. Karabutov, and A. A. Oraevsky, "Sensitivity of laser opto-acoustic imaging in detection of small deeply embedded tumors," *IEEE Trans. Ultrason. Ferroelectr. Freq. Control* **5**(4), 981–988 (1999).
29. S. L. Jacques and B. W. Pogue "Tutorial on diffuse light transport," *J. Biomed. Opt.* **13**(4), 041302 (2008).
30. S. Manohar et al., "Photoacoustic mammography with a flat detection geometry," in *Photoacoustic Imaging and Spectroscopy*, L. V. Wang, Ed., pp. 431–442, CRC Press, Boca Raton, FL (2009).
31. R.P. S. Astorga, "Haemoglobin sensing with optical spectroscopy during minimally invasive procedures," Phd Thesis, University College London (2015).
32. F. Slaghekke et al., "Fetoscopic laser coagulation of the vascular equator versus selective coagulation for twin-to-twin transfusion syndrome: an open-label randomised controlled trial," *Lancet* **383**, 2144 (2014).
33. G. M. Hale and M. R. Querry, "Optical constants of water in the 200-nm to 200-μm wavelength region," *Appl. Opt.* **12**(3), 555–563 (1973).
34. J. Su et al., "Photoacoustic imaging of clinical metal needles in tissue," *J. Biomed. Opt.* **15**(2), 021309 (2010).
35. S. L. Jacques, "Optical properties of biological tissues: a review," *Phys. Med. Biol.* **58**, R37–R61 (2013).
36. R. Nachabé et al., "Estimation of lipid and water concentrations in scattering media with diffuse optical spectroscopy from 900 to 1600 nm," *J. Biomed. Opt.* **15**(3), 037015 (2010).
37. M. Jaeger, J. C. Bamber, and M. Frenz, "Clutter elimination for deep clinical optoacoustic imaging using localised vibration tagging (LOVIT)," *Photoacoustics* **1**(2), 19–29 (2013).
38. E. J. Alles, M. Jaeger, and J. C. Bamber, "Photoacoustic clutter reduction using short-lag spatial coherence weighted imaging," in *IEEE Int. Ultrasonics Symp.*, pp. 41–44 (2014).
39. ANSI, Z136.1-2007.
40. T. M. Baran and T. H. Foster, "Comparison of flat cleaved and cylindrical diffusing fibers as treatment sources for interstitial photodynamic therapy," *Med. Phys.* **41**, 022701 (2014).

41. V. P. Zharov et al., "In vivo photoacoustic flow cytometry for monitoring of circulating single cancer cells and contrast agents," *Opt. Lett.* **31**(24), 3623–3625 (2006).
42. Y. Wang et al., "Photoacoustic imaging with deconvolution algorithm," *Phys. Med. Biol.* **49**(14), 3117 (2004).
43. J. Prakash et al., "Basis pursuit deconvolution for improving model-based reconstructed images in photoacoustic tomography," *Biomed. Opt. Express* **5**(5), 1363–1377 (2014).
44. G. Marquez et al., "Anisotropy in the absorption and scattering spectra of chicken breast tissue," *Appl. Opt.* **37**(4), 798–804 (1998).
45. V. Ntziachristos and D. Razansky, "Molecular imaging by means of multispectral optoacoustic tomography (MSOT)," *Chem. Rev.* **110**, 2783–2794 (2010).
46. B. Cox et al., "Quantitative spectroscopic photoacoustic imaging: a review," *J. Biomed. Opt.* **17**(6), 061202 (2012).
47. S. A. Steigman et al., "Optical properties of human amniotic fluid: implications for videofetoscopic surgery," *Fetal Diagn. Ther.* **27**(2), 87–90 (2010).

Biographies for the authors are not available.